

# OHS: OH-Airglow Suppressor for the Subaru Telescope

Fumihide IWAMURO,<sup>1</sup> Kentaro MOTOHARA,<sup>2</sup> Toshinori MAIHARA,<sup>3</sup>  
Ryuji HATA,<sup>1</sup> and Takashi HARASHIMA,<sup>1</sup>

<sup>1</sup> Department of Physics, Kyoto University, Kitashirakawa, Kyoto 606-8502  
iwamuro@cr.scphys.kyoto-u.ac.jp

<sup>2</sup> Subaru Telescope, National Astronomical Observatory, 650 North Aohoku Place, Hilo, HI 96720, USA

<sup>3</sup> Department of Astronomy, Kyoto University, Kitashirakawa, Kyoto 606-8502

(Received 2000 October 26; accepted 2000 November 28)

## Abstract

This paper describes an OH-airglow Suppressor (OHS) for the infrared Nasmyth focus of the Subaru telescope. OHS has the capability of eliminating 224 airglow-lines in the *J*- and *H*-bands, which are major sources of background radiation at near-infrared wavelengths up to 2  $\mu$ m. Specifically, it is a pre-optics system installed between the telescope and an infrared camera/spectrograph (CISCO). The suppressor reduces sky background emissions to 1/25 and its throughput is 40%. As a result, the S/N gain achieved with OHS is more than 1 mag compared to the typical spectroscopic approach. The limiting magnitude measured during a test observing run was found to be  $H = 21.1$  mag ( $\lambda/\Delta\lambda = 210$ , S/N = 5) in the standard 4000 s exposure sequence.

**Key words:** cosmology: observations — instrumentation: spectrographs — infrared: general

## 1. Introduction

Rapid progress has continued to be made in the study of the high-redshift universe over the last decade by the development of telescopes, large-format arrays, and observation techniques. To date, a considerable number of high- $z$  galaxies have been spectroscopically identified, and the nature of these galaxies has been investigated, mainly using their broad-band colors. However, it is impossible to separate the effects of age and extinction only from these colors. This problem has prevented the exact features of high- $z$  objects from being obtained. More detailed information — rest-frame optical spectra — is required for further studying these objects.

Although it is extremely difficult to obtain the rest-frame optical spectra of distant galaxies, several groups have succeeded in detecting some emission lines of high- $z$  radio galaxies (Eales, Rawlings 1993, 1996; Evans 1998) and of Ly break galaxies (Pettini et al. 1998) in the near-infrared *J*- to *K*-bands. Two antithetical concepts can be seen in their results. One is a lower spectral resolution to detect a faint continuum and to achieve a wider wavelength coverage; the other is a higher spectral resolution to avoid the effects of strong airglow-lines. OHS is an instrument that can merge these two concepts, achieving a high sensitivity for a faint continuum and a wide spectral coverage.

Before designing OHS for the Subaru telescope, we worked forwards confirming the basic performance of the

suppressor by using a proto-type instrument (Iwamuro et al. 1994) from 1992 to 1995 in the University of Hawaii's 2.2 m telescope on Mauna Kea. The total design of OHS described here is based on our experience from these test observations. After that, we developed an infrared camera/spectrograph (CISCO: Motohara et al. 1998) as the back-end instrument of OHS, and OHS itself was mounted on the Nasmyth stage of the Subaru telescope at the end of 1999.

The optical design and mechanical design of OHS are described in sections 2 and 3, the details of the airglow mask are reported in section 4, and the performance of the OHS/CISCO system during its first nine months of operation is summarized in section 5.

## 2. Optical Design

Figure 1 shows the optical layout of OHS. The focal ratio of the infrared Nasmyth focus of the Subaru telescope is  $f/13.2$  with the image rotator. As the figure shows, incident rays coming through the entrance slit in the gap of the two gratings are reflected by the collimator mirror, upper grating, camera mirror, mask mirror, camera mirror again, lower grating, refocus mirror, and pick-off mirror. Here, the incident beam, including the sky background and the object flux, is dispersed by the upper grating and is focused onto the mask mirror, where a bar-code-like mask is installed. This mask absorbs al-

most all airglow-lines; the remaining parts are reflected and re-combined by the lower grating. The upper layer (from the entrance slit to the mask mirror) and the lower layer (from the mask mirror to the pick-off mirror) must be separated to pick out the refocused slit image from the optical path between the refocus mirror and the entrance slit without attenuation.

This configuration also reduces the contribution of scattered light from bright incident beam before airglow rejection to the final image. Any optical aberration caused by the spherical camera mirror is reduced by the collimator mirror and the refocus mirror with their hyperbolic surfaces. However, the separation between the upper and lower layers is still restricted, i.e., the size of the entrance slit is 15 mm (28'') long by 0.5 mm (0.''93) or 0.25 mm (0.''47) wide (see section 3).

The upper and lower gratings have exactly the same optical parameters: 245 lines  $\text{mm}^{-1}$  and a blaze angle of  $37^\circ$ . These gratings disperse and then re-combine *J*-band (1.11–1.35  $\mu\text{m}$ ) and *H*-band (1.48–1.80  $\mu\text{m}$ ) light with the order of fourth and third, respectively. The dispersed *J*- and *H*-band light is focused onto the mask mirror simultaneously by a large spherical camera mirror 1.3 m in diameter. The spectral resolution on the mask mirror is  $\lambda/\Delta\lambda = 5500$  for a 0.''93 slit (and double for a narrower slit), while the rejection resolution is 3900, because the element of the mask is 1.4-times wider than the slit image (see section 4). Figure 2 shows spot diagrams at the end of the OHS optics and on the mask mirror. Since the slit length is quite small compared with the focal length of the collimator, the spot size is almost fixed inside the slit. The aspheric corrector plates placed in front of the gratings can reduce the spot size noticeably, but can also cause a lower throughput and ghost airglow images on the mask mirror, posing a serious problem for the OHS concept. The squares in the spot diagrams correspond to the pixel scale of CISCO (0.''105); the optical aberration in CISCO (Motohara et al. 1998) is slightly larger than these squares. Accordingly, the optical aberration in OHS does not have a large effect on the final image.

### 3. Mechanical Design

All of the optical elements of OHS are equipped in the upper frame supported by three hydraulic jacks on the base frame, which allows the direction of the instrument to be adjusted (figure 3). The base frame is also slidable to the waiting position by hand, despite a total weight of 3000 kg and a size of 5m  $\times$  3m. The entrance slit, the gratings, and the pickoff mirror supports are mounted on the retractable stage, which is drawn back at the waiting position to avoid any collision with the structure of the telescope. The entrance slit has five positions: pinhole, narrower (0.''47  $\times$  28'') slit, wider (0.''93  $\times$  28'')

slit, open (20''  $\times$  28''), and close. The collimator/refocus mirror support and mask mirror support are mounted on the adjustable stages driven by stepper motors along the optical axis. The dispersion power on the mask mirror can be tuned to the scale of the airglow mask by adjusting the position of the mask mirror along the optical axis, because the separation between dispersed beams changes as the position is moved (see figure 1). The airglow mask focus is adjusted by moving the position of the collimator mirror. Since these adjustments can be done only for real airglow-lines, the positions of these elements are controlled from the observation room.

CISCO is supported by an adjustable stage featuring three electric jacks and three sliding or rotating stages (figure 4). CISCO is also used as a general infrared camera with a field of view of 1.8 square attached to the Nasmyth focus directly with this adjustable stage (after OHS is moved to the waiting position). We can adjust the direction of the optical axis and the position of the camera, whichever the stage is placed.

### 4. Airglow Mask

The airglow mask is made of a thin stainless-steel plate 0.2 mm thick, and processed by photochemical etching (figure 5). The surface of the mask is coated with special black paint, which absorbs more than 99.9% of all near-infrared light up to 2  $\mu\text{m}$ . A total of 224 OH and O<sub>2</sub> airglow-lines in the *J*- and *H*-bands are rejected here, while the effective opening area is 74.4%. The width of the element of the mask is 0.7 mm, which is a factor 1.4 times the width of the slit image of 0.5 mm (this is because there may be small differences between real airglow-lines and the position of the mask element). The mask has overlapping patterns of airglow-lines in the *J*- and *H*-bands with different orders of the grating. Although this configuration is not favorable considering the instrumental throughput, we can obtain airglow-suppressed spectra in both bands simultaneously. From this point of view, we do not reject all broad molecular oxygen lines near 1.28  $\mu\text{m}$ ; this rejection requires a very wide mask for complete removal.

The wavelength of the OH-airglow emission lines was calculated from the transition levels of the OH radical reported by Coxon (1980), and Coxon, Foster (1982). The judgment of whether to reject the lines or not was made by referring to the airglow spectra observed in Maihara et al. (1993). The airglow lines rejected by this airglow mask are listed in table 1.

### 5. Test Observations and Verified Performance

Following the installation of OHS at the end of 1999, test observation runs were carried out about every two months. In this section, we first summarize the results of

these observations, and then describe the performance of this system, verified by several spectra of faint objects.

The typical observation procedure starts from what we call the “imaging mode”, in which the slit of OHS is opened and CISCO is operated as an infrared camera (figure 6). The airglow-suppressed area corresponds to the black stripe at the center of the sky image, called the “dark lane”, where the airglow-lines are in phase with the airglow mask. The effective area of the dark lane is  $1.^{\circ}3 \times 28''$ . After an object is guided into this area, about a dozen frames are taken by nodding the telescope along the dark lane between the exposure sequences. These frames are used not only for photometry, but also to confirm the object location in the dark lane at each nodding position. Next, the observation mode is switched to what is called the “spectroscopic mode”, in which the slit of OHS is moved to the center of the dark lane; in CISCO, the width of the variable slit is reduced and the  $JH$ -band grism is selected. A standard exposure time of 1000 s reaches the background-limited condition with multiple-readouts of six-times the detector. At least four exposures should be made to avoid bad pixels and unexpected hot pixels; accordingly, the standard exposure time comes to be more than 4000 s.

The total system efficiency was measured through observations of the UKIRT faint-standard stars in the imaging mode. The efficiency was 8.3% in the  $J$ -band and 12.2% in the  $H$ -band. The throughput of the OHS part was estimated to be 40% in both bands by a comparison of the throughput with and without OHS.

The spectroscopic images taken by OHS are compared with images taken by the direct spectroscopy of CISCO in figure 7. The observable spectral range for the CISCO  $JH$ -band spectroscopy is from  $1.044 \mu\text{m}$  to  $1.816 \mu\text{m}$ , which is limited by the order sorting filter paired with the grism, while the range becomes discontinuous with OHS, because the light out of either end of the mask mirror does not reach the detector. Almost all airglow-lines, except for broad  $O_2$  lines in the  $J$ -band, are rejected by OHS; this is also shown in figure 8. The rejection factor of the airglow-lines is 25.

The gain of OHS is illustrated in the lower half of figure 7. The object is radio galaxy 4C +40.36 ( $z = 2.269$ ) as observed by CISCO (May 24) and by CISCO with OHS (May 23). It is quite obvious that OHS has a large advantage in terms of sensitivity for faint objects, even with a shorter exposure time. Since the object and background flux are in proportion to  $\eta$  and  $\eta/f_s$ , respectively ( $\eta$ : throughput,  $f_s$ : suppression factor), the gain of OHS is estimated simply by

$$Gain = \frac{\eta}{\sqrt{\frac{\eta}{f_s}}} = \sqrt{\eta f_s}. \quad (1)$$

The estimated gain becomes 3.16 or 1.25 mag from the

measured values of  $\eta = 0.4$  and  $f_s = 25$ . The contribution of the read noise to the total background noise is about 10% in the case of 1000 s exposure; accordingly, the actual gain, including the read noise, is 2.87 or 1.15 mag. The limiting magnitude, as confirmed by test observations, is  $H = 21.1$  mag ( $\lambda/\Delta\lambda = 210$ ,  $S/N = 5$ ) in the standard 4000 s exposure sequence with a  $0.^{\circ}93$  slit.

Figure 9 shows spectroscopic images of several faint objects taken with OHS during the last test observation run. In these images, the noisy regions between the bands contain no data. This is because OHS throughput corrections are applied using the spectroscopic standard stars observed just after each object. Table 2 summarizes the specifications and performance. Actually, many radio galaxies and quasars have already been observed by the OHS/CISCO system, and excellent performance levels have been exhibited, not only for emission lines, but also for continuum features, through the observations.

The present results were accomplished during a test observation run of the Subaru telescope. We are therefore indebted to all members of the Subaru Observatory, NAOJ, Japan. We would like to express our thanks to the engineering staff of Mitsubishi Electric Co. for their fine operation of the telescope. This work was also supported by a Grant-in-Aid for Scientific Research (B), Japan (No. 11440065).

## References

Coxon, J. A. 1980, Can. J. Phys., 58, 933  
 Coxon, J. A., & Foster S. C. 1982, Can. J. Phys., 60, 41  
 Eales, S. A., & Rawlings, S. 1993, ApJ, 411, 67  
 Eales, S. A., & Rawlings, S. 1996, ApJ, 460, 68  
 Evans, A. S. 1998, ApJ, 498, 553  
 Iwamuro, F., Maihara, T., Oya, S., Tsukamoto, H., Hall, D. N. B., Cowie, L. L., Tokunaga, A. T., & Pickles, A. J. 1994, PASJ, 46, 515  
 Maihara, T., Iwamuro, F., Yamashita, T., Hall, D. N. B., Cowie, L. L., Tokunaga, A. T., & Pickles, A. 1993, PASP, 105, 940  
 Motohara, K., Maihara, T., Iwamuro, F., Oya, S., Imanishi, M., Terada, H., Goto, M., Iwai, J. et al. 1998, Proc. SPIE, 3354, 659  
 Pettini, M., Kellogg, M., Steidel, C. C., Dickinson, M., Adelberger, K. L., & Giavalisco, M. 1998, ApJ, 508, 539

Table 1. List of targeted airglow-lines.

Line	$\lambda$ ( $\mu\text{m}$ )	Line	$\lambda$ ( $\mu\text{m}$ )	Line	$\lambda$ ( $\mu\text{m}$ )	Line	$\lambda$ ( $\mu\text{m}$ )
OH(3-1)R1(1)	1.48877	OH(5-3)Q1(2)	1.67088	OH(5-3)P2(6)	1.73511	OH(10-7)Q1(3)	1.49850
OH(3-1)R2(1)	1.49319	OH(5-3)Q2(2)	1.67026	OH(5-3)P1(7)	1.75294	OH(5-2)P1(5)	1.10900
OH(3-1)R1(2)	1.48331	OH(5-3)Q1(3)	1.67325	OH(5-3)P2(7)	1.75012	OH(5-2)P2(5)	1.10724
OH(3-1)R2(2)	1.48644	OH(5-3)Q2(3)	1.67247	OH(5-3)P1(8)	1.76855	OH(5-2)P1(6)	1.11560
OH(3-1)R1(3)	1.47837	OH(5-3)Q1(4)	1.67636	OH(6-4)P1(2)	1.78802	OH(5-2)P2(6)	1.11409
OH(3-1)R2(3)	1.48058	OH(5-3)Q1(5)	1.68024	OH(6-4)P2(2)	1.78115	OH(5-2)P1(7)	1.12279
OH(4-2)R1(1)	1.56549	OH(6-4)Q1(1)	1.76532	OH(6-4)P1(3)	1.79939	OH(6-3)P1(2)	1.15388
OH(4-2)R2(1)	1.57025	OH(6-4)Q2(1)	1.76498	OH(6-4)P2(3)	1.79347	OH(6-3)P1(3)	1.15917
OH(4-2)R1(2)	1.55977	OH(6-4)Q1(2)	1.76718	OH(6-3)R1(1)	1.13542	OH(6-3)P2(3)	1.15652
OH(4-2)R2(2)	1.56316	OH(6-4)Q2(2)	1.76649	OH(6-3)R2(1)	1.13771	OH(6-3)P1(4)	1.16507
OH(4-2)R1(3)	1.55461	OH(6-4)Q1(3)	1.76984	OH(6-3)R1(2)	1.13312	OH(6-3)P2(4)	1.16278
OH(4-2)R2(3)	1.55702	OH(6-4)Q2(3)	1.76896	OH(6-3)R2(2)	1.13469	OH(6-3)P1(5)	1.17161
OH(4-2)R1(4)	1.55009	OH(6-4)Q1(4)	1.77334	OH(6-3)R1(3)	1.13128	OH(6-3)P2(5)	1.16963
OH(4-2)R2(4)	1.55179	OH(6-4)Q1(5)	1.77771	OH(6-3)R2(3)	1.13234	OH(6-3)P1(6)	1.17880
OH(4-2)R1(5)	1.54621	OH(2-0)P1(5)	1.47998	OH(6-3)R1(4)	1.12994	OH(6-3)P2(6)	1.17708
OH(4-2)R2(5)	1.54742	OH(2-0)P2(5)	1.47724	OH(6-3)R2(4)	1.13063	OH(6-3)P1(7)	1.18665
OH(4-2)R1(6)	1.54302	OH(2-0)P1(6)	1.49090	OH(6-3)R1(5)	1.12912	OH(7-4)P1(2)	1.22292
OH(5-3)R1(1)	1.65024	OH(2-0)P2(6)	1.48862	OH(7-4)R1(1)	1.20308	OH(7-4)P2(2)	1.21964
OH(5-3)R2(1)	1.65538	OH(2-0)P1(7)	1.50261	OH(7-4)R2(1)	1.20559	OH(7-4)P1(3)	1.22869
OH(5-3)R1(2)	1.64421	OH(2-0)P2(7)	1.50067	OH(7-4)R1(2)	1.20070	OH(7-4)P2(3)	1.22577
OH(5-3)R2(2)	1.64790	OH(2-0)P1(8)	1.51510	OH(7-4)R2(2)	1.20242	OH(7-4)P1(4)	1.23515
OH(5-3)R1(3)	1.63885	OH(3-1)P1(2)	1.52410	OH(7-4)R1(3)	1.19886	OH(7-4)P2(4)	1.23259
OH(5-3)R2(3)	1.64147	OH(3-1)P2(2)	1.51871	OH(7-4)R2(3)	1.20001	OH(7-4)P1(5)	1.24233
OH(5-3)R1(4)	1.63418	OH(3-1)P1(3)	1.53324	OH(7-4)R1(4)	1.19758	OH(7-4)P2(5)	1.24008
OH(5-3)R2(4)	1.63604	OH(3-1)P2(3)	1.52878	OH(7-4)R2(4)	1.19833	OH(7-4)P1(6)	1.25024
OH(5-3)R1(5)	1.63023	OH(3-1)P1(4)	1.54322	OH(7-4)R1(5)	1.19688	OH(7-4)P2(6)	1.24827
OH(5-3)R2(5)	1.63155	OH(3-1)P2(4)	1.53953	OH(8-5)R1(1)	1.28070	OH(7-4)P1(7)	1.25890
OH(5-3)R1(6)	1.62703	OH(3-1)P1(5)	1.55403	OH(8-5)R2(1)	1.28346	OH(8-5)P1(2)	1.30217
OH(6-4)R1(1)	1.74499	OH(3-1)P2(5)	1.55098	OH(8-5)R1(2)	1.27826	OH(8-5)P2(2)	1.29857
OH(6-4)R2(1)	1.75059	OH(3-1)P1(6)	1.56570	OH(8-5)R2(2)	1.28016	OH(8-5)P1(3)	1.30853
OH(6-4)R1(2)	1.73867	OH(3-1)P2(6)	1.56313	OH(8-5)R1(3)	1.27644	OH(8-5)P2(3)	1.30528
OH(6-4)R2(2)	1.74270	OH(3-1)P1(7)	1.57821	OH(8-5)R2(3)	1.27772	OH(8-5)P1(4)	1.31568
OH(6-4)R1(3)	1.73308	OH(3-1)P2(7)	1.57603	OH(8-5)R1(4)	1.27528	OH(8-5)P2(4)	1.31279
OH(6-4)R2(3)	1.73597	OH(3-1)P1(8)	1.59159	OH(8-5)R2(4)	1.27611	OH(8-5)P1(5)	1.32365
OH(6-4)R1(4)	1.72829	OH(4-2)P1(2)	1.60309	OH(8-5)R1(5)	1.27480	OH(8-5)P2(5)	1.32109
OH(6-4)R2(4)	1.73034	OH(4-2)P2(2)	1.59726	OH(6-3)Q1(1)	1.14399	OH(8-5)P1(6)	1.33247
OH(6-4)R1(5)	1.72431	OH(4-2)P1(3)	1.61286	OH(6-3)Q2(1)	1.14378	OH(8-5)P2(6)	1.33020
OH(6-4)R2(5)	1.72576	OH(4-2)P2(3)	1.60797	OH(6-3)Q1(2)	1.14516	OH(8-5)P1(7)	1.34216
OH(6-4)R1(6)	1.72117	OH(4-2)P1(4)	1.62354	OH(6-3)Q2(2)	1.14472	OH(8-5)P2(7)	1.34013
OH(6-4)R2(6)	1.72220	OH(4-2)P2(4)	1.61946	OH(6-3)Q1(3)	1.14683	OH(8-5)P1(8)	1.35274
OH(6-4)R1(7)	1.71891	OH(4-2)P1(5)	1.63513	OH(6-3)Q1(4)	1.14903	O2	1.26850
OH(6-4)R1(8)	1.71753	OH(4-2)P2(5)	1.63172	OH(7-4)Q1(1)	1.21226	O2	1.26875
OH(3-1)Q1(1)	1.50555	OH(4-2)P1(6)	1.64765	OH(7-4)Q2(1)	1.21204	O2	1.26900
OH(3-1)Q2(1)	1.50529	OH(4-2)P2(6)	1.64476	OH(7-4)Q1(2)	1.21359	O2	1.26925
OH(3-1)Q1(2)	1.50690	OH(4-2)P1(7)	1.66110	OH(7-4)Q2(2)	1.21311	O2	1.26950
OH(3-1)Q2(2)	1.50640	OH(4-2)P2(7)	1.65863	OH(7-4)Q1(3)	1.21549	O2	1.26975
OH(3-1)Q1(3)	1.50883	OH(4-2)P1(8)	1.67551	OH(7-4)Q1(4)	1.21799	O2	1.27000
OH(3-1)Q1(4)	1.51137	OH(5-3)P1(2)	1.69037	OH(8-5)Q1(1)	1.29057	O2	1.27095
OH(4-2)Q1(1)	1.58333	OH(5-3)P2(2)	1.68405	OH(8-5)Q2(1)	1.29036	O2	1.27260
OH(4-2)Q2(1)	1.58303	OH(5-3)P1(3)	1.70087	OH(8-5)Q1(2)	1.29212	O2	1.27460
OH(4-2)Q1(2)	1.58482	OH(5-3)P2(3)	1.69551	OH(8-5)Q2(2)	1.29159	O2	1.27955
OH(4-2)Q2(2)	1.58425	OH(5-3)P1(4)	1.71236	OH(8-5)Q1(3)	1.29432	O2	1.28245
OH(4-2)Q1(3)	1.58693	OH(5-3)P2(4)	1.70783	OH(8-5)Q1(4)	1.29722	O2	1.28450
OH(4-2)Q1(4)	1.58973	OH(5-3)P1(5)	1.72486	OH(10-7)Q1(1)	1.49302	O2	1.28660
OH(5-3)Q1(1)	1.66924	OH(5-3)P2(5)	1.72103	OH(10-7)Q2(1)	1.49294	O2	1.58045
OH(5-3)Q2(1)	1.66892	OH(5-3)P1(6)	1.73838	OH(10-7)Q1(2)	1.49528	O2	1.58085

Table 2. Specifications and performance.

Wavelength coverage	1.477–1.804 $\mu\text{m}$ ( <i>H</i> -band), 1.108–1.353 $\mu\text{m}$ ( <i>J</i> -band)
Slit size	0. <sup>9</sup> 93 or 0. <sup>47</sup> $\times$ 28 <sup>''</sup>
Throughput	40%
Suppression factor	25
Gain by OHS	2.87 (1.15 mag)
Total system efficiency	12.2% ( <i>H</i> -band), 8.3% ( <i>J</i> -band)
Final spectral resolution	210 or 420
Limiting magnitude	<i>H</i> = 21.1 mag (S/N = 5, 4000 s)

Fig. 1.. Optical design layout of OHS. The focal lengths of all of the concave mirrors are 2000 mm, and the centers of curvature of the camera and the mask mirrors are at the same position as the center of the entrance slit.

Fig. 2.. Spot diagrams at 1.48, 1.56, 1.64, 1.72, and 1.80  $\mu\text{m}$  in the *H*-band. The diagrams in the *J*-band are exactly the same as those in the *H*-band because their differences are equivalent to the order of the gratings. The squares of 56  $\mu\text{m}$  correspond to the pixel scale of CISCO (0.<sup>105</sup> at the Nasmyth focus). a) Refocused spot image at the end of the OHS part, where the entrance slit of CISCO is located. b) Spot images on the mask mirror. The width of the element of the mask is 700  $\mu\text{m}$  (see section 4).

Fig. 3.. Assembly drawing of OHS.

Fig. 4.. Photograph of the OHS/CISCO system mounted on the Nasmyth focus of the Subaru telescope. CISCO is positioned to the side of OHS, at the top left in this photograph.



Fig. 5.. Airglow mask made of a thin stainless-steel plate 0.2 mm thick. This mask has overlapping patterns of airglow-lines in the *J*- and *H*-bands, and the effective opening area is 74.4%.

Fig. 6.. Blank-sky image taken in the imaging mode. The field of view in this mode is 20<sup>''</sup>  $\times$  28<sup>''</sup> and the airglow-suppressed area corresponds to the black stripe at the center of this image.

Fig. 7.. Comparison between CISCO direct spectroscopy and the OHS/CISCO system. a–c) Airglow spectra (a) taken by CISCO, (b) taken by the OHS/CISCO system, and (c) multiplied by 5. d–f) Reduced spectra of the radio galaxy 4C +40.36 ( $z = 2.27$ ) (d) taken by CISCO with 1200 s exposure, (e) taken by the OHS/CISCO system with 800 s exposure, and (f) taken by the OHS/CISCO system with 3200 s exposure. Five emission lines can be detected, i.e., [O II] 3727, [Ne III] 3869, H $\beta$ , and [O III] 4959/5007.

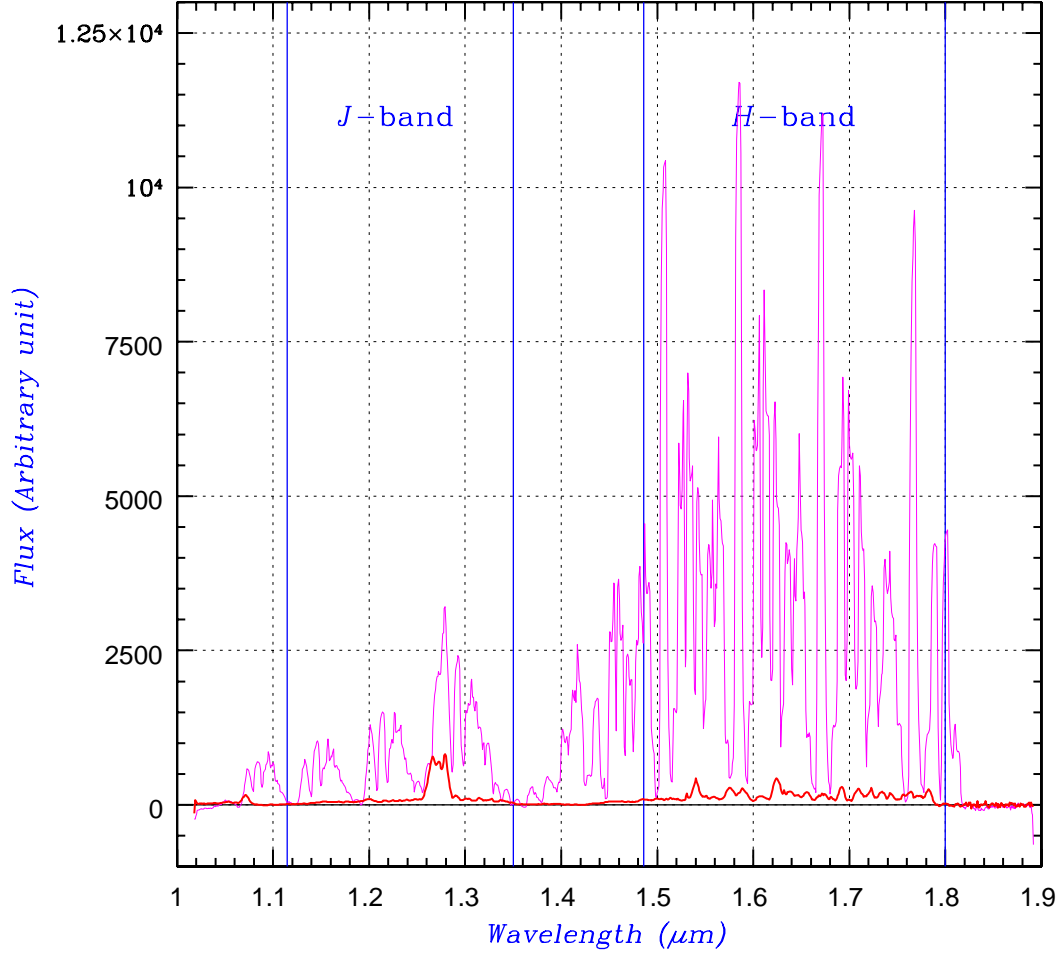


Fig. 8.. Airglow spectra with and without OHS. The throughput of OHS (40%) is corrected and the rejection factor of the airglow-lines is 30 except the region of the broad O<sub>2</sub> lines at  $\sim 1.28\mu\text{m}$ . The vertical lines indicate the observable spectral range with OHS.

Fig. 9.. *H*-band images (left) and *JH*-band spectra (right) of several faint objects. a) Radio galaxy MRC 0156–252 ( $H = 18.45$ ,  $z = 2.025$ , 4000 s) with a spectacular “[O III] jet”. b) SDSSp J021102.72–000910.3 ( $H = 18.75$ ,  $z = 4.895$ , 6000 s) with a very broad Mg II emission. c) Radio galaxy MRC 0406–244 SE ( $H = 19.11$ ,  $z = 2.428$ , 6000 s) with a knot structure. d) An ERO candidate ( $H = 19.75$ ,  $z = \text{unknown}$ , 6000 s). e) BTM98 cK39W/E ( $H = 20.89$ ,  $z = 2.434$ , 5000 s) with [O II] and [O III] emission lines. f) MLG93 G2 ( $H = 22.04$ ,  $z = 3.429$ , 8000 s) with strong [O II] and [Ne III] lines.

This figure "fig1.gif" is available in "gif" format from:

<http://arxiv.org/ps/astro-ph/0101076v2>

This figure "fig2.gif" is available in "gif" format from:

<http://arxiv.org/ps/astro-ph/0101076v2>

This figure "fig3.gif" is available in "gif" format from:

<http://arxiv.org/ps/astro-ph/0101076v2>

This figure "fig4.jpg" is available in "jpg" format from:

<http://arxiv.org/ps/astro-ph/0101076v2>

This figure "fig6.gif" is available in "gif" format from:

<http://arxiv.org/ps/astro-ph/0101076v2>

This figure "fig7.gif" is available in "gif" format from:

<http://arxiv.org/ps/astro-ph/0101076v2>

This figure "fig9.gif" is available in "gif" format from:

<http://arxiv.org/ps/astro-ph/0101076v2>